Continental Shelf Research 28 (2008) 1316–1332

Contents lists available at ScienceDirect

Continental Shelf Research

journal homepage: www.elsevier.com/locate/csr

Longshore transport estimation and inter-annual variability at a high-energy dissipative beach: St. Trojan beach, SW Oléron Island, France

Xavier Bertin [a,b,*], Bruno Castelle [c,d], Eric Chaumillon [b], Rémi Butel [e], Robin Quique [b]

[a] National Civil Engineering Laboratory, Estuaries and Coastal Zones Division, Avenida do Brasil 101, 1700-066 Lisbon, Portugal
[b] Centre Littoral De Géophysique, Université de La Rochelle, Avenue Michel Crépeau, 17042 La Rochelle Cedex 1, France
[c] UMR CNRS EPOC-5805, Université de Bordeaux I, Avenue des Facultés, 33405 Talence Cedex, France
[d] Griffith Centre for Coastal Management, Gold Coast Campus, Griffith University, PMB 50 Gold Coast Mail Centre, Qld 9726, Australia
[e] IMB, Université Bordeaux I, 351 Cours de la Libération, 33405 Talence Cedex, France

ARTICLE INFO

Article history:
Received 5 July 2007
Received in revised form
7 February 2008
Accepted 13 March 2008
Available online 15 March 2008

Keywords:
Longshore transport
Dissipative beach
Fluorescent tracers
Wave-induced currents
Numerical model

ABSTRACT

This study investigates the annual and inter-annual longshore transport at a high-energy dissipative beach (St. Trojan, SW Oléron Island, France), over the period 1997–2006. This study is divided in two parts: (1) a short-term study, based on field measurements carried out during, low, moderate and high-energy swell conditions, and permitting to calibrate a wave propagation model and both empirical longshore sediment transport formulas and a hydro-sedimentary numerical model; and (2) a long-term study, combining global optimization methods using WAVEWATCH III (WW3) model outputs and wave numerical modelling to define the nearshore wave climate and then to compute the annual and inter-annual longshore transport. A good agreement between the different methods was obtained and values for the annual longshore transport ranged from about $50{,}000 \pm 20{,}000\,m^3$/yr to $140{,}000 \pm 30{,}000\,m^3$/yr. The net annual longshore transport displayed an inter-annual variability, whereas values were always 3–10 times less than those proposed in previous studies. Such differences point out the necessity of calibrating empirical transport formulas and computing accurately the nearshore wave climate. The relatively low values for the net annual longshore transport were explained by a weak contribution of the most energetic swells, which systematically approach the shore with a frontal obliquity and also generate episodes of reverse transport. The methodology itself was also discussed, pointing out the limitations of this study but also the advantages of using WW3 data and simplified wave climates.

1. Introduction

Wave-dominated beaches are some of the most dynamic features around the world coastlines. Improvement in field measurement techniques together with multidisciplinary approaches (naturalist, physical and numerical) have led to a strong improvement of the knowledge of these environments for the last decade. Wave-dominated beaches display a great variability in their morphology, attributed by Masselink and Short (1993) to the combination of the wave energy (wave height and period), the sediment grain size and the tidal range. Amongst the different classes of beaches defined by Masselink and Short (1993), many studies have been conducted on low tide terrace beaches (Ciavola et al., 1997; Ferreira et al., 2000; Balouin et al., 2005), on macrotidal ridge and runnel beaches (Levoy et al., 1998; Masselink and Anthony, 2001) and low tide bar/rip beaches (Masselink and Hegge, 1995; Pedreros et al., 1996; Castelle et al., 2006a). On the contrary, the literature concerning the dynamic of non-barred dissipative beaches is relatively poor and is only restricted to some quantitative studies (Wright et al., 1979; Russel, 1993).

Amongst the different processes that govern the dynamics of wave-dominated beaches, longshore transport is one of the most important and interests not only the scientific community, but also coastal managers and engineers (White, 1998). Various methods have been used in order to estimate the longshore transport and can be classified in two main categories: field measurement methods and physical/numerical/empirical methods. Field measurement methods include sediment traps (Schoonees and Theron, 1993), radioactive tracers (Inman and Chamberlain, 1959; Long and Drapeau, 1985; Pruszak and Zeidler, 1994), fluorescent tracers (Ingle, 1966; Kraus et al., 1982; Ciavola et al., 1997; Levoy et al., 1998; Ferreira et al., 2000; Vila-Concejo et al., 2004; Balouin et al., 2005; Tonk and Masselink, 2005), optics (Dowing et al., 1981) and acoustics (Osborne and Vincent, 1996). Longshore transport empirical formulas were developed in the 1980's and namely include the CERC (1984), the Bailard (1984)

* Corresponding author. National Civil Engineering Laboratory, Estuaries and Coastal Zones Division, Avenida do Brasil 101, 1700-066 Lisbon, Portugal.
E-mail addresses: xbertin@lnec.pt (X. Bertin), b.castelle@epoc.u-bordeaux1.fr (B. Castelle), remi.butel@math.u-bordeaux1.fr (R. Butel).

0278-4343/$ - see front matter © 2008 Elsevier Ltd. All rights reserved.
doi:10.1016/j.csr.2008.03.005

and the Kamphuis (1991) formulas. Empirical formulas remain an interesting tool for estimating longshore transport, as attested their use in recent studies (Abadie et al., 2006; Balouin et al., 2005; Park and Wells, 2005; Tonk and Masselink, 2005) or the recent development of the new Kaczmarek et al.'s (2005) formula. Nevertheless, White (1998) pointed out that such formulas often result in error larger than the predicted transport rate while numerical models non-calibrated with field data provide results which can differ by orders of magnitude with measurements. In addition, the gap between the longshore transport at the hydrodynamic event time scale (i.e., one swell event) and the annual longshore transport rate implies a good knowledge of the annual nearshore wave climate and is often difficult to fill in. These weaknesses are particularly problematic for high-energy environments, since accurate field data are lacking for those environments, namely for annual transport rates larger than 200,000 m^3 and wave heights greater than 1.8 m (Schoonees and Theron, 1993; Taborda et al., 1994). Consequently, some of the values to be found in the literature for the annual longshore transport might comport some weaknesses such as: (1) a non-calibration of transport formulas; (2) an inaccurate determination of wave angle at breaking; and (3) a simplified annual nearshore wave climate. In the perspective of a better understanding of wave-dominated coastal systems, these weaknesses need to be addressed and some of the values for annual longshore transport should be revisited using modern tools, such as accurate wave records, sediment transport data and numerical models.

It is the purpose of this study to present a complete methodology which aims at estimating the annual longshore transport at a high-energy dissipative beach. The first part of this study presents short-term measurements of waves, wave-induced currents and sand transport deduced from tracers for three different hydrodynamic settings. These data are used to calibrate a wave propagation model, a hydro-sedimentary model and empirical formulas. The correlation between measured and predicted sand transport is discussed at the end of this first section. The second part of this study presents the method used to compute the annual and inter-annual longshore transports. WAVEWATCH III (WW3) model outputs and global optimization techniques are used to define a simplified offshore wave climate and the nearshore wave climate is obtained from the wave propagation model. Annual and inter-annual longshore transports are obtained using the hydro-sedimentary model and empirical formulas, calibrated from the short-term study and forced by the nearshore wave climate. A discussion about the computed annual longshore transport is finally provided.

2. The study area

2.1. Geomorphology

The study area is located in the middle part of the Atlantic coast of France. The continental shelf extends 120 km offshore and displays a very low gradient (1–2/1000). The study area is located within the middle of the 8 km-long beach that develops in the southwestern part of Oléron Island (Fig. 1). This part of the Island is made of unconsolidated sediments and corresponds to a large sandy spit where aeolian dunes are well developed. This beach is mainly made of fine and well-sorted sands ($D_{50} = 0.18$–0.22 mm), which together with the energetic wave climate implies high values for the surf scale parameter Ω. According to the classification proposed by Masselink and Short (1993), these high values for Ω suggest this beach is more likely to develop a non-barred dissipative morphology. This theoretically predicted morphology is coherent with field observations and with the results of the bathymetric survey carried out in April 2005, which showed (Fig. 1): (1) the absence of large subtidal bedforms; (2) the absence of large intertidal bedforms; and (3) an overall lightly concave and low gradient beach profile, with a relatively constant gradient within the intertidal zone ($\tan\beta = 0.015$). Still in agreement with Masselink and Short's (1993) classification, small amplitude intertidal bar/rip structures appear only after several weeks of fair weather conditions, like during the summer months.

2.2. Hydrodynamics

The tide affecting the study area is semi-diurnal and ranges from less than 2 m during neap to more than 5 m during spring tides (macrotidal). Associated tidal currents are strong within the tidal inlet located to the south (>2 m/s; Bertin et al., 2004, 2005) but very weak at the studied beach and non-significant in comparison with wave-induced currents. Maximum tidal current velocities at the studied beach were simulated with a depth-averaged flow model (Bertin et al., 2005) and never exceed 0.05 m/s up to 500 m of the shoreline within a spring/neap tidal cycle. Such velocities are unable to put sand into motion within the studied beach, thus tidal action is restricted to water level variation.

Long-term wave data available for the study area are non-continuous and non-directional. Consequently, wave data considered in this study were obtained from the National Centers for Environmental Prediction (NCEP) online archives (http://polar.ncep.noaa.gov/waves). The data used in this study corresponds to a simulation point (46°N, 2.5°W) of the WW3 numerical model (Tolman et al., 2002; Tolman, 2002), located 90 km to the WNW of the studied beach (Fig. 1), and available every 3 h since 1997. A good correlation between measurements and the predictions of this model was already demonstrated in the Bay of Biscay (Butel et al., 2002; Abadie et al., 2005, 2006). A statistical analysis of the WW3 data between 1997 and 2005 provides a general description of the offshore wave climate (Fig. 2):

(1) Waves amplitude $1\,\mathrm{m} < H_s < 2\,\mathrm{m}$ are predominant and represent more than 60% of the annual wave climate while waves with $H_s > 5$ m represent about 3%.
(2) Peak wave period $8\,\mathrm{s} < T_p < 12\,\mathrm{s}$ are predominant and represent close to 60% of the annual wave climate while waves with $T_p > 15$ s occur about 2% of the time.
(3) Wave direction is predominantly W to NW, which represents close to 60% of the wave climate (Fig. 2) while the largest swells have systematically a W direction (265–275°N).

The predominant WNW wave direction results in a dominant southerly littoral drift at the study area. Using empirical formulas, Baxères (1978) and Bellessort and Migniot (1987) have proposed the net littoral drift to be in the order of 500,000 m^3/yr. It is one of the purposes of this paper to re-examine this value.

3. Method

In order to address the complex question of the annual longshore transport estimation at this dissipative beach, a combination of different methods was used in this study. Field experiments, including bathymetric surveys, fluorescent tracers and hydrodynamic measurements, were conducted to estimate longshore transport for three distinct hydrodynamic settings representative of the annual wave climate and to calibrate a wave propagation model and a hydro-sedimentary model. A global optimization method was then applied to offshore WW3 outputs

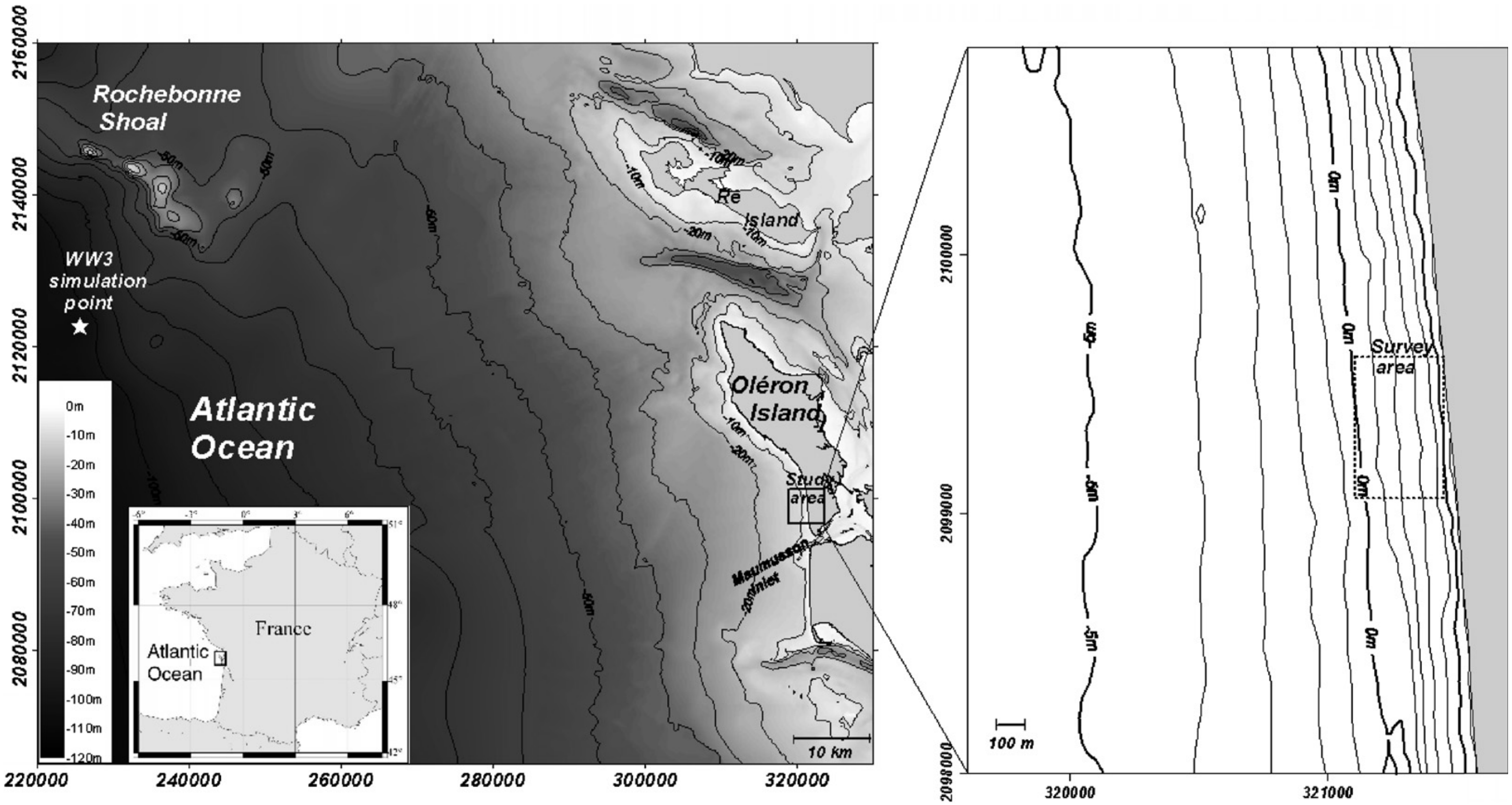

Fig. 1. General location of the study area, bathymetric interval is 10 m and WW3 simulation point where the annual wave data were extracted. Detailed bathymetric map of the studied beach, surveyed in April 2005, and showing its dissipative morphology. For both maps, Lambert II coordinates are in metres.

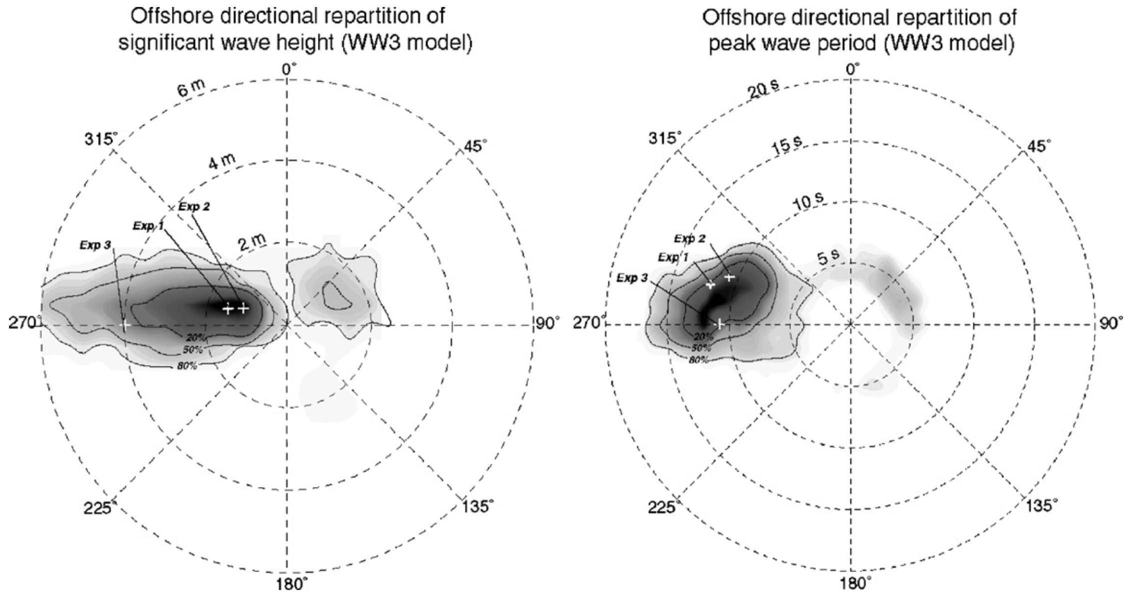

Fig. 2. Offshore directional repartition of significant wave height and peak wave period, showing a clear dominance of W to NW swells.

and combined with regional wave modelling, to define simplified annual and inter-annual nearshore wave climates. Finally, empirical transport formulas were forced both by this simplified nearshore wave climate and by the time series of wave parameters, in order to compute the annual longshore transport. For computational reasons, the hydro-sedimentary model was forced only by the simplified nearshore wave climate.

3.1. Bathymetric data

The beach morphology was surveyed by using a combination of a hydrographic survey at high tide and overlapping a topographic survey at low tide, the latter also being used to check the reliability of the bathymetric measurements. The St. Trojan beach was surveyed on 4 April 2005 using a Septentrio® Polar X2 Real Time Kinematic GPS, the mobile antenna of which was mounted on a bicycle. The accuracy of this GPS is about 1 cm in the horizontal and 2 cm in the vertical direction. The shoreface of the beach was surveyed on 1 April 2005 at high tide by the local hydrographic office (Direction Départementale de l'Equipement 17). The original position data, acquired in WGS 84 format, were converted into Lambert II planar and metric coordinates, this being the working coordinate system used throughout the study.

3.2. Fluorescent tracer

Five hundred kilograms of natural sand were collected within the middle of the intertidal area at St. Trojan beach. This sand was cleaned with fresh water, dried in the open air and tagged using an orange paint at a ratio of 5 kg paint per 100 kg sand. The tagged sand was dried in the open air and sieved using a 1-mm mesh to remove aggregates; the grain-size distribution of the tracer was controlled and was found to be very close to natural sand. Before injection on the beach, the tracer was washed with a detergent solution in order to eliminate surface tension and to avoid associated grain-floating problems.

Following the recommendations of White (1998), preliminary investigations were conducted on the beach in order to determine the sand mixing depth Z_0 for different wave height conditions and are detailed in Bertin et al. (2008). The values ranged from 1.5 to 5 cm depending on wave height, accordingly to the relation proposed by Ferreira et al. (2000). The depth of the traps where the tracers were injected was adjusted according to the Z_0-values, together with the swell forecast before each experiment. Constancy of Z_0 within the beach during each experience was checked by analysing core samples collected within the middle of each sampling profile. Considering such low values for the sand mixing depth, a simple "one layer" model was chosen to interpret the tracer experiments, according to Kraus (1985) "river of sand" model. It means that the sand was assumed to move as a uniform layer of thickness Z_0 at the velocity U_c (U_{cx}, U_{cy}). The transport velocity U_c (U_{cx}, U_{cy}) is defined as the movement of tracer cloud centroïd C (X_c, Y_c) between two successive low tides, divided by the time of submersion t_i, according to the spatial integration method of White and Inman (1989):

$$U_{cx} = \frac{X_c - X_0}{t_i}, \tag{1}$$

$$U_{cy} = \frac{Y_c - Y_0}{t_i}. \tag{2}$$

The tracer cloud centroid in the two dimensions X and Y and is given by

$$X_c = \frac{\sum_{k=1}^{k=n} C_k x_k}{\sum_{k=1}^{k=n} C_k}, \tag{3}$$

$$Y_c = \frac{\sum_{k=1}^{k=n} C_k y_k}{\sum_{k=1}^{k=n} C_k}, \tag{4}$$

where C_k is the tracer concentration at the position k.

Finally, the sediment transport flux Q_c is given by

$$\vec{Q}_c = (1-n) Z_0 \vec{U}_c, \tag{5}$$

where n is the sediment porosity, estimated to 0.39 at the laboratory.

The percentage of remaining sand tracer after each experiment R_m, also called percentage of recovery (Ciavola et al., 1997; White, 1998; Balouin et al., 2005), was computed according to

$$R_m = \frac{100 M_d}{M_t - M_r}, \tag{6}$$

where M_t is the mass of tracer injected (kg), M_r is the mass of tracer (kg) remaining at the injection point below Z_0 and M_d is the mass of tracer (kg) detected within the sampled area.

3.3. Hydrodynamic forcing measurements

3.3.1. Instrument deployment

Instead of programming fieldwork for a fixed date, optimal swell and tide conditions have been waited for between April 2005 and March 2006. These conditions include: (1) swell displaying characteristics representative of the local wave climate conditions (Section 2.2 and Fig. 2); (2) swell displaying narrow frequency and directional spectrums, in order to measure and to accurately compute the parameters (H_s, T_p and Dir_p) to be introduced into the transport formulas; (3) light winds (<5 m/s), to be sure that sand transport is induced by swells only; and (4) a tidal range >3 m, enabling the currentmeter to be deployed at low tide and a transect of wave parameters and related-current to be obtained at mid and high tide (during the tracer immersion).

A currentmeter S4-ADW (Interocean®) was deployed in the lower part of the intertidal zone in order to record wave characteristics. Data were acquired at a 2 Hz sample rate throughout the tracer experiments. A 2D-ACM Doppler currentmeter was deployed close to the tracer injection points, in order to record wave currents at 0.4 m from the bottom. Current velocities and directions were sampled at 2 Hz and averaged on 30 s to record steady currents only.

In addition, S4-ADW data acquired to the north of Oléron Island in November 2002 (water depth of 23 m; Idier et al., 2006) constituted the only open-ocean, accurate and directional wave data available in this area. These data were used to validate the SWAN and WW3 models (Section 3.3.2).

3.3.2. Data processing

Specific Matlab® programs were developed to process the hydrodynamic data acquired during tracer experiments. The 2D-ACM currentmeter data processing only consisted in correcting the tilt effect, which attained 15° by the end of the first experiment.

Considering the S4-ADW data acquired within the surfzone, sea surface elevations were estimated assuming that the pressure field was hydrostatic, as demonstrated by Lin and Liu (1998). A first low-frequency cutoff of $F_1 = 0.04$ Hz was applied to the raw signal S_0, in order to remove tidal variations and infragravity constituents. Data processing was then performed by splitting the entire record into consecutive windowed ensembles of 600 s each. Power spectral estimates $S(f)$ were computed by Fourier transforming overlapping (75%), Hanning windowed. The significant wave height H_s (m) was defined as four times the square root of the 0th moment m_0 of the power wave spectrum $S(f)$ obtained by the integration of the energy spectra over the frequency band F_1–F_2, where F_2 is a high-frequency cutoff of 0.3 Hz. The peak wave period was computed as the frequency at which the maximum spectral energy density was to be found within the band F_1–F_2. The peak wave direction Dir_p (°) was computed from the free surface elevation (ξ) and the horizontal velocity components (u_c and v_c) using cross-spectrums $C_{xy}(f)$ according to relation (7):

$$\mathrm{Dir}_p = \arctan\left(\frac{a}{b}\right), \tag{7}$$

where $a = \max[C\xi u_c(f)]$ and $b = \max[C\xi v_c(f)]$.

Two-dimensional directional spectra were plotted using the DIWASP Matlab® package of Johnson (2002). Wave-induced currents were computed by applying low-frequency cutoffs of $F_1 = 0.04$ Hz and $F_3 = 0.0011$ Hz to the longshore (v_c) and the cross-shore (u_c) velocity components. Hereafter, these low-pass-filtered wave-induced currents are referred to as steady wave-induced currents. Since S4-ADW is an electromagnetic currentmeter, the steady wave-induced currents described in this study are local ones, at the depth of the sensor (0.4 m above sea bottom).

3.4. Determination of the nearshore wave climate

3.4.1. Statistical definition of offshore wave conditions

It has already been shown that clustering can be performed by global optimization techniques (Butel et al., 2002; Bagirov et al., 2002). The first step of the classification method is then to define the function to be minimised. The function, called total(P), is defined here as

$$\mathrm{total}(P) = \sum_{C\in P}\sum_{x\in C}\mathrm{dist}(x, C_g), \tag{8}$$

where P is any given partition of the dataset, C any class in this partition, C_g the approximated centre of gravity of class C and x any point of this class. The distance between two sea states is here defined as

$$\mathrm{dist}\left(\begin{vmatrix} H_{s1} \\ T_{p1} \\ D_{p1}\end{vmatrix}, \begin{vmatrix} H_{s2} \\ T_{p2} \\ D_{p2}\end{vmatrix}\right) = \sqrt{\frac{(H_{s2}^2 - H_{s1}^2)^2}{\sigma^2_{H_s^2}} + \frac{(T_{p2} - T_{p1})^2}{\sigma^2_{T_p}} + \frac{(D_{p2} - D_{p1})^2}{\sigma^2_{D_p}}}, \tag{9}$$

where $\sigma_{H_s^2}$, σ_{T_p} and σ_{D_p} are the significant square wave height, peak period and peak direction variances, respectively. In this study, offshore swells expected to generate a negligible or a zero longshore transport at the studied beach (i.e., swells of $H_s < 0.5$ m or swells having a eastward component) were removed. The original formulation of Butel et al. (2002) for the distance between two sea states was modified in this study by replacing H_s by H_s^2, in order to improve the representation of high-energy/short-duration swell events and to avoid their smoothing. Actually, because transport formulas are strongly non-linear, these high-energy events are expected to induce strong sediment transports. The computation of the approximated gravity centres of the classes was then performed by minimisation of the 'total' function. This minimisation was performed using the simulated annealing method of Kirkpatrick et al. (1983).

3.5. Wave propagation model

SWAN is a spectral wave model based on the wave action density balance equation (Booij et al., 1999). The version 40.41 was used in stationary mode to simulate wave propagation and deformation from deepwater up to the shallower shorelines of Oléron Island. This model was set to take into account the bottom friction (Madsen et al., 1988), wave breaking (Battjes and Janssen, 1978) and triad wave–wave interaction. Because of the relatively reduced dimensions of the modelled domain and the very low gradient of the bottom, other source terms such as quadruplet wave–wave interaction and reflection were switched off, respectively. Because of the stochastic wind characteristics (magnitude, direction) together with the long-term aspect of this study, whitecapping and wind contributions were also switched off.

The main modelled domain extends from Oléron Island to the WW3 simulation point in the E/W direction and from the Gironde Estuary to the North of Ré Island (Fig. 1) in the N/S direction. The spatial discretisation follows a regular and rectangular grid, with a mesh size of about 250 m. A local and more refined grid (mesh size of 10 m) was nested within the coarse grid, to simulate wave propagation from water depth of about 20 m up to the shoreline and to compute wave parameters at breaking to be introduced into the transport formulas. The numerical bathymetry for this latter grid was obtained by interpolating bathymetric data described in Section 3.1 on a regular grid with 20 m spacing. The spectral discretisation was done according to 15 frequencies ranging between 0.5 and 0.02 Hz. A constant spectrum was used along the offshore boundary of the coarse grid. A Gaussian-shaped frequency spectrum was used and a directional spreading of 25° was chosen. Simulations were run using the wave classes detailed in 3.3.1 as offshore forcing (108 runs). In order to check the validity of the simplified wave climate and to study the wave climate seasonal variability, the WW3 original time serie (3-h interval) was also used as offshore forcing over the period 1997–2006 (26,300 runs).

The model calibration was undertaken by adjusting an uniform friction coefficient K_n until a good comparison was obtained between modelled significant wave heights when forced by WW3 data at its boundaries and the field data available both at St. Trojan beach (Fig. 4) and to the north of Oléron Island (Fig. 3). Best agreements were obtained using $K_n = 0.065$ m, which is included in the range of values proposed by default in SWAN ($K_n = 0.05$ m) and obtained by Castelle et al. (2006a) ($K_n = 0.085$ m) for southwestern France beaches. The second aspect of the model calibration was performed within the surf zone by adjusting the breaker parameter γ in the bore-based model of Battjes and Janssen (1978). Simulations showed that the default value $\gamma = 0.73$ significantly overestimated the wave height in the surf zone. The best agreement with measured significant wave height was given by $\gamma = 0.65$, which is included within the range of values found by Battjes and Stive (1985) between 0.6 and 0.83.

Wave simulations were run according to these settings and results were output along a cross-shore profile crossing the S4 recorder. Using empirical transport formulas implies to define rigorously the location of the breaking point. Smith et al. (2003) proposed to define it as the location landward of which a fast rate of wave height decay is observed. In this study, the breaking point was defined as the point where the ratio H_s/depth reached 0.5, which is less than the value of 0.6 proposed by Abadie et al. (2006) for the steeper beaches of the southwestern France coastline. This ratio $H_s/\text{depth} = 0.5$ corresponds to a fraction of wave energy lost by breaking larger than 4–5%. Such a criterion is coherent with visual observations made during the field experiments, and also corroborates the conclusions of Bonneton (2001), which suggest weaker ratio H_s/depth for gently sloping beaches.

3.6. Sediment transport modelling

3.6.1. Empirical formulas

Several empirical transport formulas have been developed in the 80's and those used in this study are commonly used and include the CERC (1984) formula and the Kamphuis (1991) formula. Details about the use of these formulas can be easily found in the litterature (see Balouin et al., 2005). More recently, Kaczmarek et al. (2005) developed a new formula from radio-isotopic measurements, which is of the form $Q_s = f(H^2V)$, where V is the mean longshore current into the breaking zone:

$$Q_s = 0.023(H_b^2 V), \quad \text{if } (H^2V) < 0.15, \tag{10}$$

$$Q_s = 0.00225 + 0.008(H_b^2 V), \quad \text{if } (H^2V) > 0.15, \tag{11}$$

where H_s is the significant wave height (m); V is the mean longshore current, computed by the same authors with the relation:

$$V = 0.25 k_v \sqrt{\gamma g H_b} \sin 2\alpha, \tag{12}$$

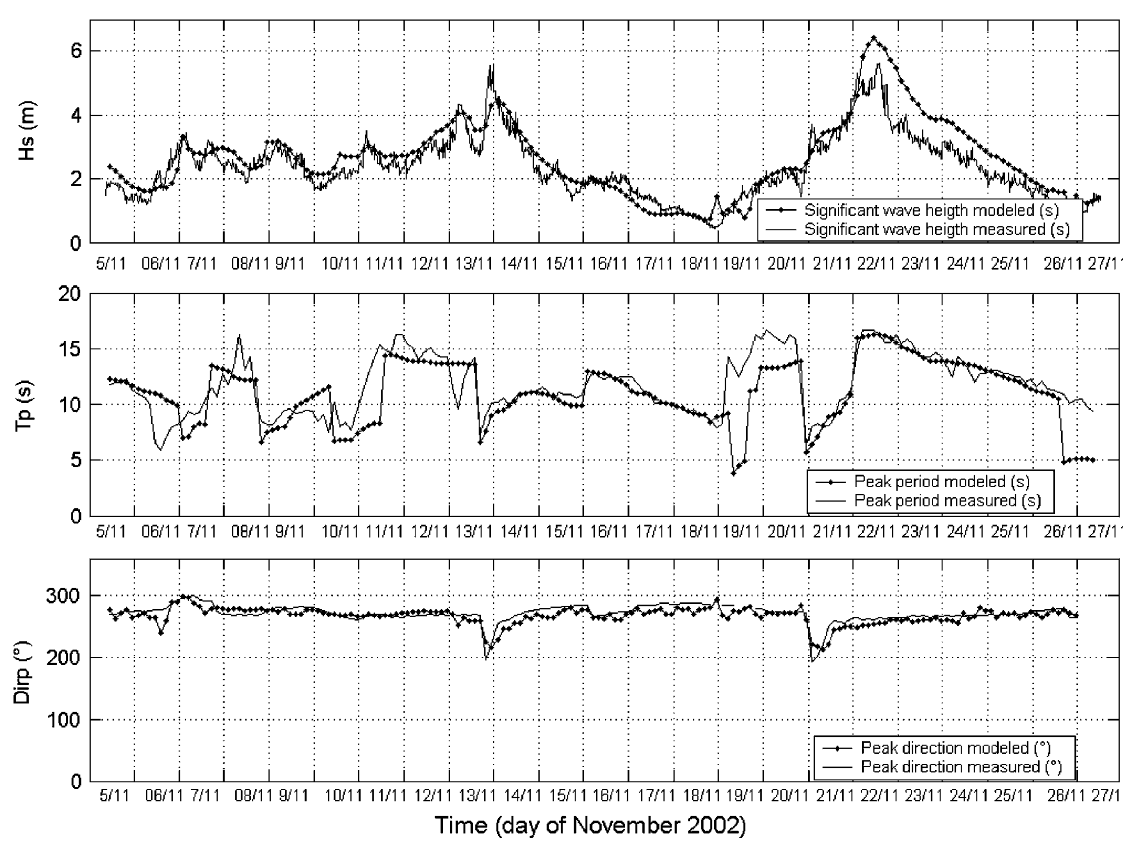

Fig. 3. Correlation between wave parameters (H_s, T_p and Dir_p) measured in November 2002 and results of the SWAN model, forced offshore by the WW3 model.

where α is the wave angle at breaking, γ is the constant breaker parameter (0.78) and k_v an empirical constant which according to the authors could have a regional validity. The value for k has been computed by combining the measured longshore current and wave parameters during field experiments. Best agreements between measured longshore current velocities and predicted ones according to relation (12) were obtained for $k_v = 2.9$, which is very close to the value proposed by Komar and Inman (1970) for the eastern coast of the USA.

3.6.2. The hydro-sedimentary numerical model

3.6.2.1. Theoritical formulation. The flow module of MORPHODYN is used herein and is detailed in Castelle et al. (2006a). It is based on time average of the depth-integrated mass and momentum conservation equations which are solved using an implicit method to obtain quasi-steady mean water depth h and water volume fluxes $\vec{Q}$.

The SWAN wave driver set and described in Section 3.3.2 (Booij et al., 1999) is used to solve the spectral action balance equation and to provide wave forcing. The wave forcing is given by the radiation stress tensor after Svendsen and Petrevru (1996) using the linear wave theory. The roller contribution is not taken into account.

The closure problem of the flow module is solved with the mixing term T_{ij}, using the Einstein notation $(i = 1,2;\ j = 1,2)$, computed with the depth-averaged eddy viscosity approach:

$$T_{ij} = \rho K_m h\left(\frac{\partial(Q_i/h)}{\partial x_j} + \frac{\partial(Q_j/h)}{\partial x_i}\right), \tag{13}$$

where ρ is the mass density of water and K_m is given by Battjes (1975):

$$K_m = Mh\left(\frac{D}{\rho}\right)^{1/3} + v_0, \tag{14}$$

where D is the rate of energy loss due to wave breaking, M a dimensionless coefficient and v_0 an empirical eddy viscosity.

Bottom shear stress is parameterized as being proportional to the mean flow through a bottom friction coefficient C_f and the wave orbital velocity near the bottom U_w, following the weak flow approximation of Liu and Dalrymple (1978):

$$\tau_i^b = \rho C_f U_w U_{c_i}, \tag{15}$$

where the mean current velocities U_{c_i} is given by the decomposition of Philipps (1977) to take into account the undertow contribution:

$$U_{c_i} = \frac{Q_i - q_i}{h}, \tag{16}$$

where q_i is the mean volume flux associated with the wave motion.

The Bailard model (Bailard, 1981) is used to compute the sediment transport field $\vec{Q}t$ due to mean currents. $\vec{Q}t$ consists of two components: the suspended and bedload transport by relatively depth-uniform mean current (respectively, $\vec{Q}b$ and $\vec{Q}s$) given by Bailard (1981):

$$\vec{Q}t = \vec{Q}b + \vec{Q}s, \tag{17}$$

with

$$\vec{Q}b = \frac{\varepsilon_b C_f}{g(s-1)\tan\Phi} U_w^2 \vec{U}_c, \tag{18}$$

$$\vec{Q}s = \frac{\varepsilon_s C_f}{g(s-1)w_s} U_w^3 \vec{U}_c, \tag{19}$$

where ε_b and ε_s are, respectively, the bedload and suspended load efficiency factors, w_s is the settling velocity, Φ is the sediment friction angle and s is the sediment porosity.

3.6.2.2. Model settings. St. Trojan beach configuration was almost alongshore-uniform during the tracer experiments 1– 3. Thus, it was chosen to use the 1DH mode of the numerical model. Wave outputs were extracted from the 10 m resolution grid on the cross-shore profile crossing the S4 location, and extending from the dune to approximately 20 m below the Lowest Astronomical Tide (LAT).

This sediment transport formulation combined with the depth- and time-averaged sediment mass conservation was successfully used to simulate the formation and the evolution of 3D rhythmic bedform features in the surf zone (Castelle et al., 2005, 2006b). However, the present sediment transport formulation is not accurate enough to simulate the cross-shore sediment transport and the resulting cross-shore movements of the sandbars (Hoefel and Elgar, 2003). Thus, the sediment transport formulation presented herein is used to estimate the longshore sediment transport only.

3.6.2.3. Model calibration. The calibration of both the wave model and the time- and depth-averaged flow model was undertaken using the S4 measurements. Comparison with the tracer experiment was used to calibrate the sediment transport module in the longshore direction. Results obtained with the different calibrated parameters are presented in Section 4. For the calibration of the flow module, we assumed that the longshore current velocity measured by the S4 (located about 0.4 m up to the bottom) was representative of the depth-averaged velocity. Best agreements were obtained with $C_f = 0.0048$ in agreement with Castelle et al. (2006a), $M = 1$ and $v_0 = 1$.

The longshore sediment transport rate was computed for the two first tracer experiments, using $C_f = 0.0048$ which is located within the range $0.0014 < C_f < 0.0358$ proposed by Bailard. Calibration consisted of tuning the sediment transport efficiency factors ε_b and ε_s (Eqs. (18) and (19)) and best results were obtained for $\varepsilon_b = 0.05$ and $\varepsilon_s = 0.01$. The values obtained in this study are weak in comparison with the confidence bound values ($0 < \varepsilon_b < 0.44$ and $0.016 < \varepsilon_b < 0.031$) of Bailard (1984).

4. The short-term studies

4.1. Hydrodynamic conditions during field experiments

According to the WW3 model, offshore swell conditions during experiment 1 were characterised by a significant wave height of $H_s = 1.60$ m, a mean peak period of $T_p = 12$ s and a peak direction of $\mathrm{Dir}_p = 285°$. At the breaking point, the measured wave conditions were characterised by a significant wave height of $H_s = 1.10$ m, a peak period of $T_p = 12.5$ s and a mean peak direction of $\mathrm{Dir}_p = 269°$, implying waves were breaking with a mean angle of about $\alpha = 5°$ with respect to the shore (Fig. 4, Table 1). Wave conditions simulated using the SWAN model were in good agreement with field measurements (Fig. 4), with a correlation coefficient $R^2 = 95$ for H_s and RMS differences at the breaking point of 0.12 m for H_s, 0.5 s for T_p and 2° for α. Directional wave spectrums show that energy was distributed over very narrow directional and frequential bands. An important quantity of energy was also found at a frequency of two times the peak period, suggesting an important development of the first order harmonic. The analysis of steady wave-induced currents (Fig. 5, Table 1) shows the presence of southward longshore with a mean maximum velocity of $v_c = 0.35$–0.45 m/s. The strongest longshore currents were observed within a band extending from the breaking zone up to water depth of about 0.5 m, and then they decreased rapidly up to the shoreline. Longshore current velocity also decreased rapidly after the breaking zone (seaward).

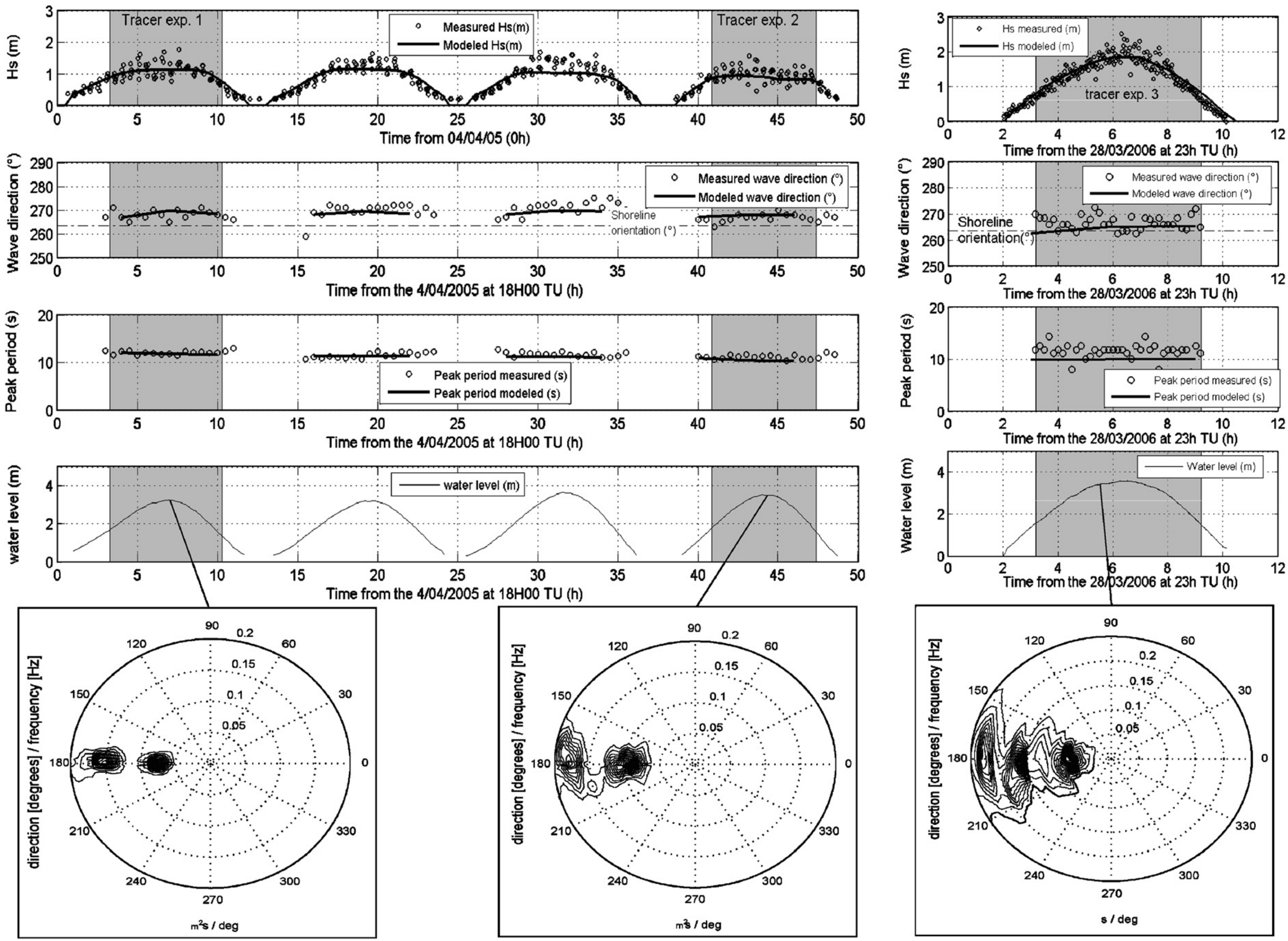

Fig. 4. Wave parameters recorded during the three tracer experiments and superimposition with the swan model prediction for H_s (a), T_p (b) and Dir_p (c). Tidal water level variations over the S4 sensor are represented in (d) and directional wave spectra during each tracer experiment, showing a strong development of the first order harmonics, are represented in (e).

Table 1
Mean wave and wave-induced current characteristics during the three tracer experiments

	Date	H_s (m)		T_p (s)		Dir (°)		Longshore velocity (m/s)	Undertow velocity (m/s)
		Offshore (WW3)	Breaking point	Offshore (WW3)	Breaking point	Offshore (WW3)	Breaking point		
Experiment 1	4–5 April 2005	1.60	1.1	12	12.5	285	269	−0.35 to −0.45	−0.15
Experiment 2	6 April 2005	1.28	0.9	10.9	11	278	268	−0.2 to −0.35	−0.15 to −0.1
Experiment 3	28–29 March 2006	4.05	2.0	10.1	11.5	270	265	0.5 to −0.4	−0.5

Current velocities correspond to mean maximal velocities, which are generally found around the breaking point.

Simulated longshore currents display a good agreement with field data, both in terms of velocity and cross-shore distribution, with a RMS of the difference of 0.09 m/s. Spectral analysis showed that longshore currents were exclusively modulated by infragravity frequencies (0.002–0.05 Hz), with main peaks at 0.02 and 0.036 Hz. Steady cross-shore current-directed offshore (undertows) were maximum around the breaking zone, where they reached −0.25 m/s. Spectral analysis shows that undertows were also modulated by infragravity frequencies (0.002–0.05 Hz), with main peaks at 0.004 and 0.02 Hz.

Experiment 2 was characterised by offshore waves with $H_s = 1.3$ m, $T_p = 11$ s, $\mathrm{Dir_p} = 278^\circ$ and at the breaking point $H_s = 0.9$ m, $T_p = 11$ s and $\mathrm{Dir_p} = 265$–272° (mean $= 268^\circ$), signifying the waves were breaking with a mean angle close to 3–4° with respect to the shore (Fig. 4, Table 1). Nearshore simulated waves display a good agreement with field data, with a correlation coefficient $R^2 = 93$ for H_s and RMS differences at the breaking point of 0.05 m for H_s, 0.8 s for T_p and 1.5° for α. Directional wave spectrums show that energy was distributed over narrow directional and frequential bands, with as for experiment 1, an important development of the first order swell harmonics. Longshore wave-induced current ranged from $v_c = -0.2$ to -0.35 m/s at the breaking point. Simulated longshore currents display a good agreement with field data for the first-half of the tidal cycle (RMS of the difference of 0.05 m/s), but not for the second-half, where the short increase in longshore velocity was not reproduced. Spectral analysis shows that longshore currents were modulated by infragravity frequencies (main peaks at 0.02 and 0.034 Hz). Undertows were maximum around the breaking point, where they reached $u_c = 0.15$–0.1 m/s. Spectral analysis shows that undertows were also modulated by infragravity frequencies with main peaks at 0.003 and 0.02 Hz.

Offshore wave conditions during experiment 3 were characterised by a significant wave height of $H_s = 4$ m, a mean peak period of $T_p = 11$ s and a peak direction of $\mathrm{Dir_p} = 270^\circ$ and at the breaking point, waves $H_s = 2$ m, a $T_p = 11$ s and a peak direction globally normal to the shore ($\mathrm{Dir_p} = 263$–272°; Fig. 4, Table 1). As for the two first experiments, wave conditions simulated using the SWAN model were in very good agreement with field measurements, with a correlation coefficient $R^2 = 97$ for H_s and RMS differences at the breaking point of 0.10 m for H_s, 1.5 s for T_p and 2.6° for α. Longshore wave-induced currents were alternatively northward and southward-directed and mean maximum values ranged from $v_c = -0.50$ to +0.4 m/s (Fig. 5). Unlike experiments 1 and 2, simulated longshore currents were of the right order of magnitude but their successive inversions of direction during the second-half of the tidal cycle were not reproduced by the model, which resulted in a bad RMS of the difference (0.28 m/s). As for experiences 1 and 2, longshore current velocities were strongly modulated by infragravity frequencies, with a peak energy at 0.004 Hz. Undertows increased from the shoreline to the breaking point where they established to $u_c = 0.5$ m/s with peak values reaching almost 1 m/s. Undertows were thus often stronger than longshore currents and were also modulated by infragravity frequencies, with a main peak at 0.005 Hz.

4.2. Tracer experiments

During experiment 1, the tracer experienced about 7 h of wave action and spread over a cloud of 120 m longshore by 100 m cross-shore (Fig. 6). The percentage of remaining fluorescent tracer R_m was found to be in the order 82%, confirming validity of this experiment (Table 2). The tracer cloud centroid moved 16 m cross-shore and 29 m longshore (southward) and within a layer of 0.033 m. The corresponding computed longshore velocity was $U_{cy} = -1.16 \times 10^{-3}$ m/s. The cross-shore integration of this sand movement results in a longshore transport of $Q_{cy} = -5.9 \times 10^{-3}$ m^3/s (506 m^3/day).

During experiment 2, the tracer also experienced 7 h of wave action but spread over a cloud of about 60 m longshore by 80 m cross-shore (Fig. 6). R_m was 73%, confirming the validity of this second experiment (Table 2). The tracer cloud centroid moved 5 m cross-shore and 15 m longshore (southward) and the sand mixing depth was about 0.025 m. The corresponding computed longshore velocity was $U_{cy} = -0.6 \times 10^{-3}$ m/s. The cross-shore integration of this sand movement results in a longshore transport of $Q_{cy} = -2.5 \times 10^{-3}$ m^3/s (213 m^3/day).

During experiment 3, the tracer experienced about 6.5 h of wave action. A first qualitative investigation was carried out on the beach with a portable UV lamp, aiming at determining the cloud extension and dimensioning the sampling grid, and did not allow for recovering tracer in significative quantities. This was confirmed by the quantitative analysis of the samples, which revealed that tracer concentrations were two orders of magnitude less than during two first experiments, causing the recovery rate to be in the order of 18%, that was insufficient to valid this experiment (Fig. 6, Table 2). Consequently, no longshore transport was computed from this third tracer experiment.

4.3. Comparison between tracer, model and empirical formula results

The values for the wave parameters at breaking were computed from the SWAN model (forced by WW3) during each tracer experiment and were then introduced into the different empirical formulas and the numerical model (Fig. 7). An error margin was also taken into account for each parameter and was arbitrary defined as the standard deviation between the wave model results and wave measurements. This error margin was of about 10% for H_s and 4% for T_p, which implies an excellent correlation between wave model results and measurements for these two parameters. The error margin for the wave angle at breaking was of the order of 1.5–2°, but mainly resulted from a

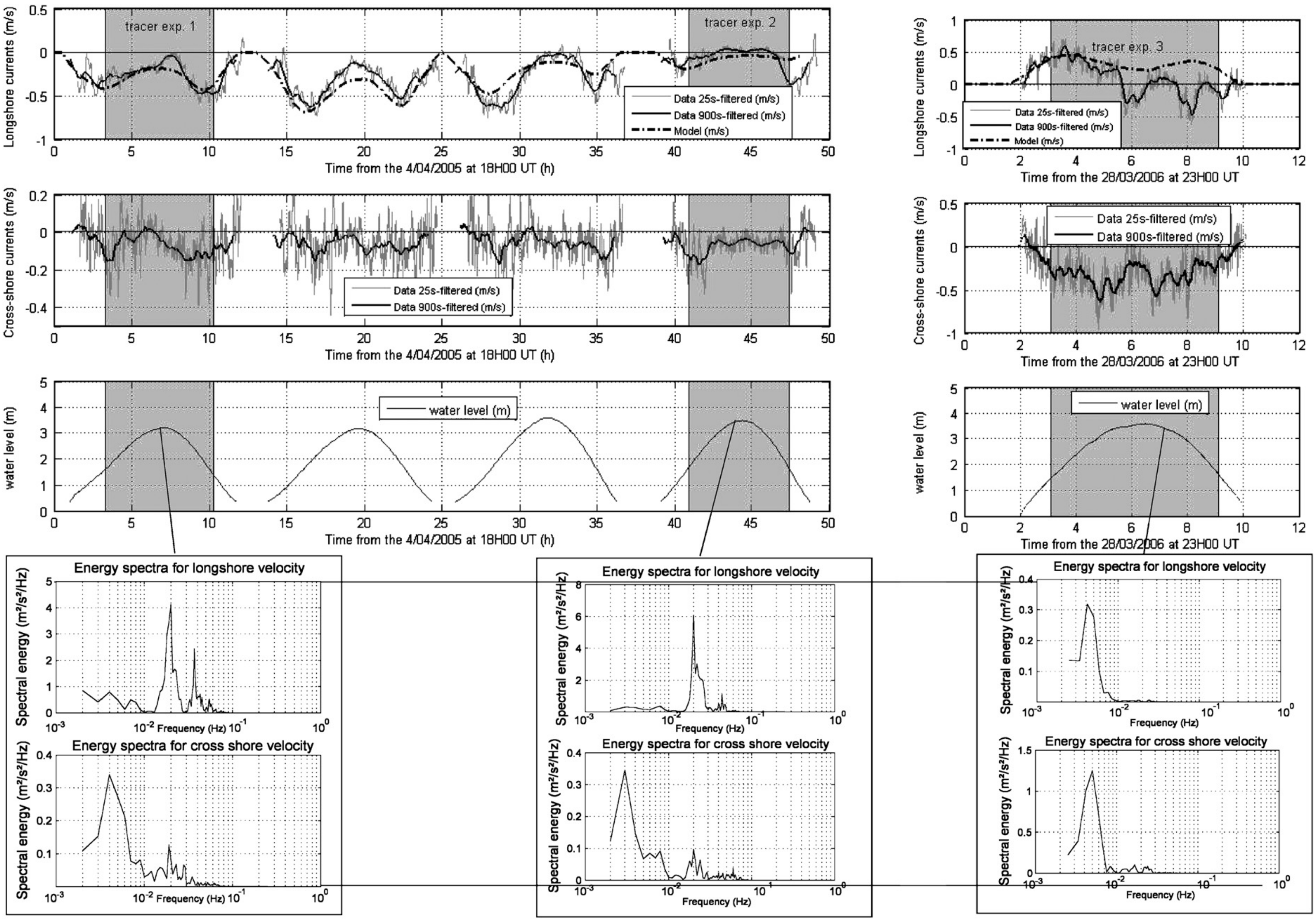

Fig. 5. Permanent wave-induced currents at the S4-ADW sensor, recorded during the three tracer experiments a simulation by the numerical model, with: (a) longshore current velocity and (b) cross-shore current velocity. Energy spectra for: (d) longshore velocity ($m^2/s^2/H_s$) and (e) cross-shore velocity ($m^2/s^2/H_s$), showing their strong modulation by infragravity frequencies.

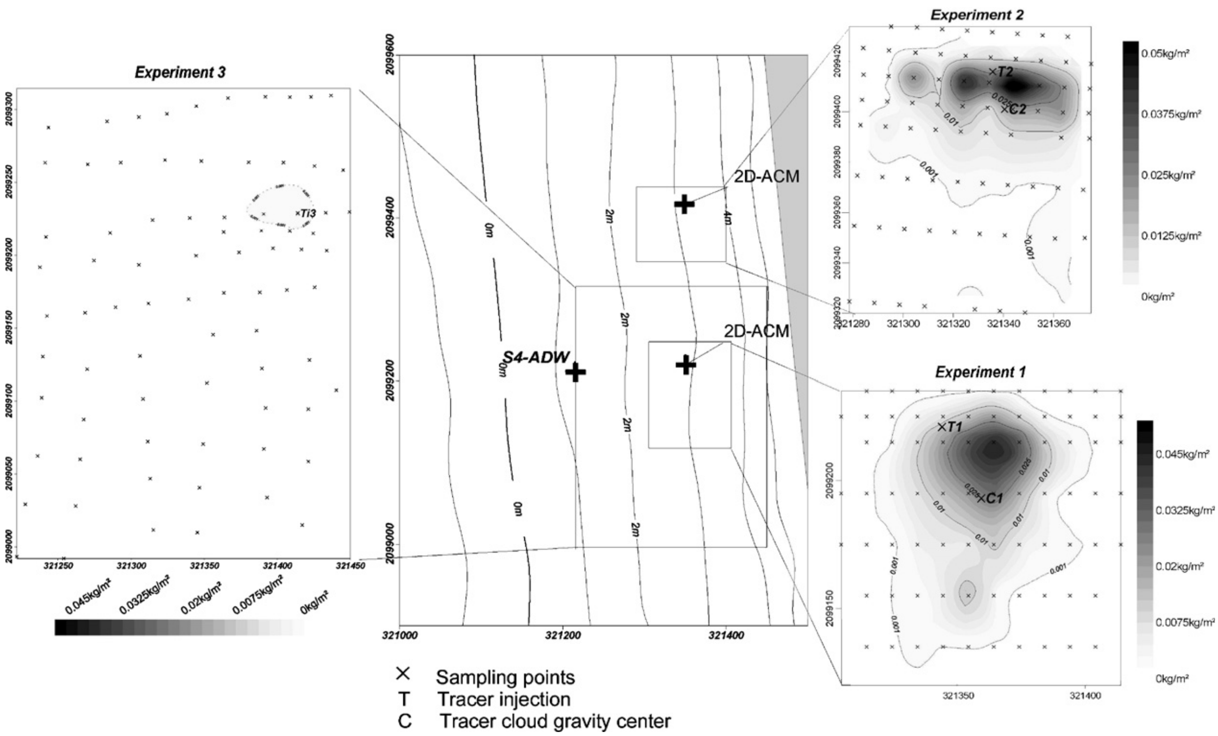

Fig. 6. Tracer dispersion and localisation map for the three tracer experiments (tracer concentration in kg of tracer/m^2) with Lambert II coordinates in metres.

Table 2
Computation of the recovery rate and validation for each experiments

	Date	Mass of tracer injected (M_t)	Mass of tracer remaining at the release point (M_r)	Mass of tracer detected outside the release point (M_d)	Mixing depth (m)	Recovery rate (%)	Validation of experiment
Experiment 1	4–5 April 2005	170	89	66.5	0.035	82	Yes
Experiment 2	6 April 2005	100	29	51.6	0.025	73	Yes
Experiment 3	28–29 March 2006	138 kg	80	10.2	0.05	18	No

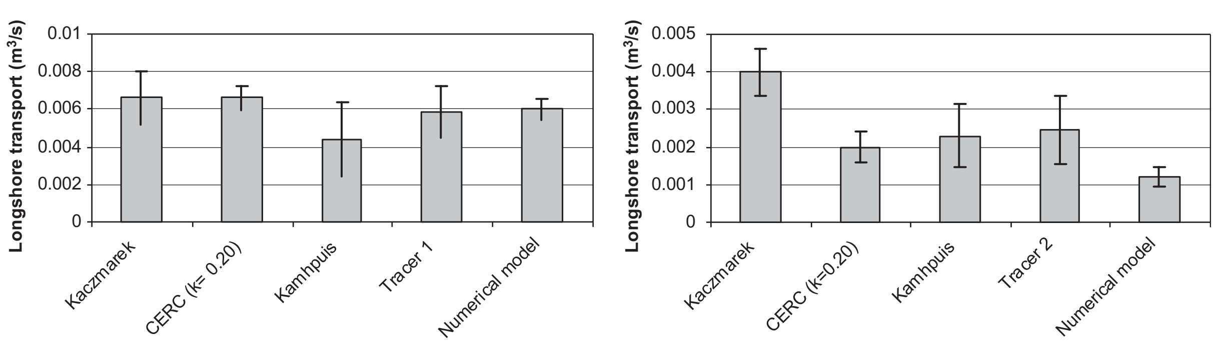

Fig. 7. Comparison between longshore transport deduced from tracers and longshore transport predicted by the CERC (1984), the Kamphuis (1991) and the Kaczmarek et al. (2005) empirical formulas and by the numerical model, for the two first tracer experiments.

dispersion of wave angles around their mean value. Nevertheless, when compared to the small wave angle at breaking (typically 5°), such an error rapidly becomes the main error source for estimating longshore transport with empirical formulas.

The most difficult formula to be used is the CERC (1984) formula, since the predicted transport rate strongly depends on the value chosen for the K empirical coefficient, which ranges from 0.21 to 0.98 according to the authors (Kraus et al., 1982; Kamphuis, 1991; Michel, 1997; Ciavola et al., 1997; US Army Corps of Engineers, 1998; Balouin et al., 2005). A value of 0.20 was selected and results in good agreements with the transport rates deduced from the tracer experiments.

Considering the transport rates deduced from tracer experiments as the most reliable ones and given the large error margins, the transport rates predicted by the Kaczmarek et al. (2005) formula, the CERC (1984) formula, the Kamphuis (1991) formula and the numerical model are in relatively good agreements for the two experiments. In more details, the Kamphuis (1991) formula seems to sligthly underestimate the transport while the Kaczmarek et al. (2005) formula seems to slightly overestimate it. For the first experiment, values range from $0.0044 \pm 0.0014\,m^3/s$ to $0.0070 \pm 0.0020\,m^3/s$ and for the second experiment, values range from $0.0016 \pm 0.0005\,m^3/s$ to $0.0030 \pm 0.0005\,m^3/s$.

4.4. Correlation between hydrodynamics and sediment transport

Waves of moderate energy ($H_s = 1.10\,m$) breaking slightly obliquely (5°) during experiment 1 induced moderate longshore currents, which could explain the large longshore extension of the tracer cloud. According to the numerical model, longshore transport consisted of a comparable part of bedload and suspension transport. While bedload transport could be directly related to the presence of moderate longshore transport, suspension transport could originate from the combination of wave orbital motions and wave breaking putting sand into suspension and longshore current advecting it. The moderate cross-shore extension of the tracer cloud could be due to the combination of wave skewness, wave breaking and undertows.

Lower energy waves ($H_s = 0.9\,m$) of experiment 2, breaking more normally (3–4°) induced weak longshore currents (mean = 0.2–0.35 m/s). These weak longshore currents could explain why the tracer cloud displayed a weaker longshore extension. According to the numerical model, suspended longshore transport was two times larger than bedload transport. This relatively larger suspended transport could be explained by the presence of moderate orbital motions putting sand in suspension, while this sand could then be advected by longshore currents. The larger cross-shore extension of the tracer cloud could be explained by a dominance of cross-shore processes (wave breaking, wave skewness and undertows).

High-energy wave ($H_s = 2\,m$) of experiment 3, breaking quasi-normally with respect to the shore induced steady offshore-directed currents that were often exceeding longshore currents. This hydrodynamic setting could be responsible for important offshore-directed sand transport associated to a high diffusion of the tracer, explaining why the tracer concentrations to be found on the beach were very weak. The subsequent bad recovery rate of this experiment has prevented from any transport computation and this points out the challenge that represents the success of tracer experiments during high-energy wave conditions.

5. The long-term study: annual and inter-annual variability of longshore transport

5.1. The annual nearshore wave climate

Annual representative wave classes have been computed for each year from 1997 to 2005 WW3 data, using the classification method presented in Section 3.4.1. Table 3 gives an example of how this method permits 1 year of wave data to be condensed into only 12 representative swell classes. For each year, two main swell categories can be distinguished within offshore wave classes: (A) low to moderate WNW swell conditions, representing 58–69% of the annual wave climate and where $H_s = 0.8$–$2.5\,m$, $T_p = 6$–$12\,s$ and $Dir_p = 274$–292°N; (B) energetic W swell conditions, representing 15–27% of the annual wave climate and where $H_s = 2.5$–$9.4\,m$, $T_p = 11$–$15\,s$ and $Dir_p = 265$–280°N. Looking to the original WW3 time series, it can be seen that swells of category (A) occur mostly during summer months (June to September), while swells of category (B) occur mostly during winter months (November–March) and spring and autumn are characterised by a transition between these two wave regimes.

Swell deformations during their propagation from the outer continental shelf to the study area was simulated for each wave class using the SWAN model (Booij et al., 1999), tuned as described in Section 3.3.2. Swell deformation combines refraction to an attenuation of amplitude (example for year 1999 in Table 1). Accordingly to the linear wave theory, the most energetic swells (category B) experienced the strongest deformations, that include an amplitude attenuation, which can exceeds 50% (Fig. 10, classes 8 and 10 and experiment 3 in the short-term study), and a strong refraction that caused them to approach the shore quasi-normally (−4° to 5° of incidence). On the contrary, less energetic swells of category (A) are subjected to lower deformations, including a weaker attenuation (10–20%) together with a smaller refraction, which permit them to reach the coast with angle attaining up to 10–13° (Fig. 10, classes 2). The simulation of wave propagation for the whole time series between 1997 and 2006 provides the demonstration for the seasonal variability of the nearshore wave climate (Fig. 8). A strong contrast can be observed between summers characterised by low energy waves ($H_s = 0.5$–$1\,m$, $T_p = 5$–$10\,s$) breaking more obliquely (5–10° of incidence) and winters characterised by energetic waves ($H_s = 1.5$–$2\,m$, $T_p = 10$–$15\,s$) breaking quasi-normally (−4° to 5° of incidence).

Table 3
Example of wave classes computed from the WW3 data by means of the simulated annealing method for the year 1999

Category	Wave class year 1999	Annual percentage	Off-shore wave conditions (point WW3, 2.5°W; 46°N)			Wave conditions at the breaking point		
			H_s (m)	T_p (s)	Dir_p (°)	H_s (m)	T_p (s)	Dir_p (°)
(A)	1	23.56	1.10	8.8	288.9	0.77	8.8	269.9
	2	18.37	1.47	11.4	282.9	0.99	11.6	265.7
	3	13.95	2.10	10.5	283.8	1.26	10.5	267.8
	4	8.699	2.68	12.4	279.3	1.06	12.5	266.6
	5	8.047	1.88	6.2	282.7	1.06	5.2	270.8
(B)	6	7.068	3.12	8.9	278.8	1.89	8.9	268.2
	7	5.074	3.82	11.6	277.3	2.10	11.7	265.9
	8	2.247	4.58	11.9	276.0	2.36	12.1	265.1
	9	1.268	5.52	13.1	273.7	2.70	13.4	263.4
	10	0.833	6.71	13.2	270.0	3.1	13.5	261.4
	11	0.289	7.61	12.1	267.7	3.2	12.4	260.7
	12	0.072	9.48	12.5	267.5	3.4	12.8	259.7
(C)		10.5	<0.5	<5	East component			

The simulation of the propagation from the open sea up to the breaking point is shown in the Fig. 10 for the classes 2, 8 and 10.

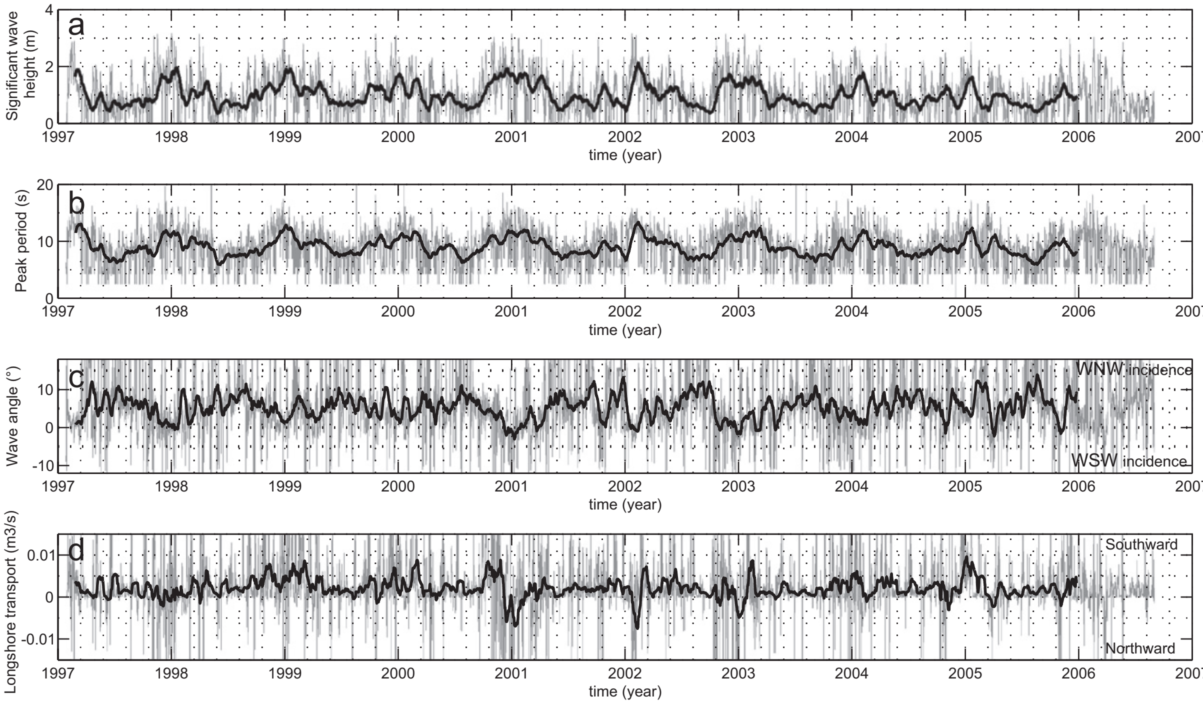

Fig. 8. Time series of wave parameters at the breaking point between 1997 and 2006: (a) significant wave height, (b) peak period, (c) wave angle and longshore transport from the CERC formula. The bold line corresponds to a 15-day filtering of these data.

5.2. Annual and inter-annual longshore transport

Wave parameters (H_s, T_p and Dir_p) at the breaking point were computed from the SWAN model (Booij et al., 1999) for each swell class from 1997, as well as for the whole time-series from 1997 to 2005. These parameters were then used to force the selected transport formulas. For computational reasons, the numerical model was forced using wave classes only, by wave outputs extracted along a cross-shore profile starting at 20 m below LAT, as described in Section 3.6.2.2. In both cases, the instantaneous longshore transport computed for each wave class was converted into annual transport considering the annual occurrence of each class. Considering model/data comparison at the breaking point did not show any particular bias, it was assumed that errors for the wave angle and the significant height at breaking were of random type. Annual values for longshore transport were thus computed taking into account an error margin on the wave angle, randomly distributed within the range $-2^\circ/+2^\circ$ according to a normal law, defined by a mean $\mu = 0$ and a variance σ^2 arbitrarily set to one. The error margin on the significant wave height at the breaking point was estimated to be 9% over the different experiments and was also included into the computation following the same procedure as for the wave angle (with $\mu = 0$ and $\sigma^2 = 5\%$).

The computation of longshore transport for the whole time-serie provides the demonstration for the seasonal variability of longshore transport (Fig. 8d). As for wave parameters (Section 5.1 and Fig. 8a–c), a contrasting situation can be evidenced between summer characterised by weak but almost always southward-directed transport and winter characterised by stronger but alternatively southward and northward-directed longshore transport. When computing the annual longhore transport for a given year and considering the large associated error margins, an overall reasonable agreement between each formula and each method (representative classes or whole time series) can be observed, permitting an inter-annual variability to be seen (Fig. 9). In more details, the Kamphuis (1991) formula gives values significantly weaker with respect to the values obtained from the CERC (1984) formula, the Kaczmarek et al. (2005) formula and the numerical model. Values range from about $50{,}000 \pm 20{,}000\,m^3/yr$ to $140{,}000 \pm 30{,}000\,m^3/yr$, with a minimum in 2000–2001–2002, located between two maximums in 1998–1999 and 2004–2005 (Fig. 9).

5.3. The causes for longshore transport "relatively" low values

The validation of empirical transport formulas from tracer experiments and their forcing by a simplified nearshore wave climate as well as by the whole time series of wave parameters has enabled to compute values for the net annual longshore transport ranging from $50{,}000 \pm 20{,}000\,m^3/yr$ to $140{,}000 \pm 30{,}000\,m^3/yr$. An inter-annual variability in longshore transport has been shown, with two peaks in 1998–1999 and 2004–2005 and a minimum in 2001. These values were bounded by large errors, which mainly originated from the error margin on the wave angle combined to the presence of low wave angles to the shore at the breaking point.

However, whatever is the formula and the year considered, these values are 3–10 times less than the previous estimations for this beach (Baxères, 1978; Bellessort and Migniot, 1987). A simple explanation could be to call into question the reliability of the results presented in our study. It can firstly be argued that conserving a constant bathymetry over all the period of this study could be an error source, especially as this beach experienced erosion. Repetitive beach profile measurements (not presented here) were carried out every year since 1997 and show that the main cross-shore variations concerned the beach upper part and the dune, while the lower part of the beach profiles are well superimposed. On a longshore point of view, dune erosion appears well homogenous at the location of this study, causing the shoreline orientation to be constant at the time-scale of this study.

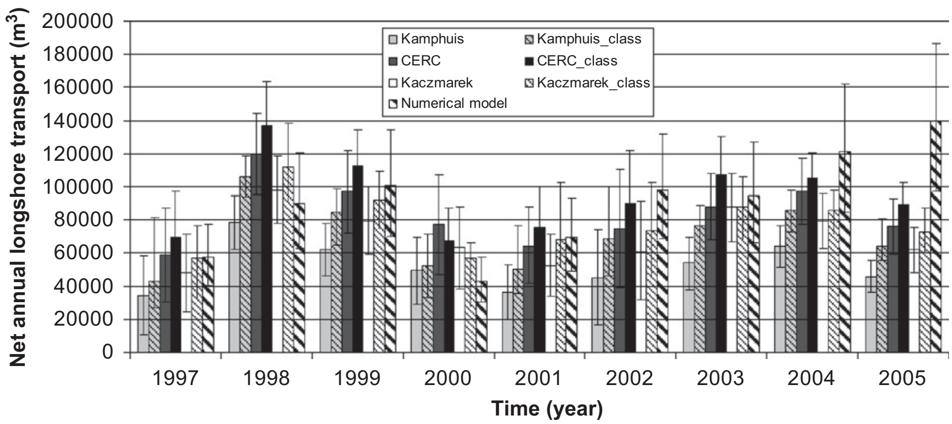

Fig. 9. Annual estimations and inter-annual variability of the longshore transport computed from the CERC (1984), the Kamphuis (1991) and the Kaczmarek et al. (2005) empirical formulas and from the numerical model, using both a simplified wave climate (wave classes) and the original WW3 time series.

Table 4
Respective contributions of low-energy (category (A)) and high-energy (category (B)) swells in the southward, the northward and net annual longshore transport

Year	Low-energy (A)		High-energy (B)		Total		Total
	Southward	Northward	Southward	Northward	Southward	Northward	Net
1997	50,630	−9952	30,785	−16,552	81,415	−26,503	54,912
1998	78,300	−8800	47,723	−14,055	126,020	−22,855	103,165
1999	85,842	−8133	49,323	−17,284	135,160	−25,418	109,742
2000	84,552	−10,822	52,473	−24,743	137,020	−35,565	101,455
2001	67,606	−11,088	25,296	−26,732	92,902	−37,820	55,082
2002	70,747	−8924	32,668	−42,340	103,410	−51,264	52,150
2003	61,739	−8819	32,180	−12,863	93,919	−21,682	72,237
2004	74,338	−11,637	42,877	−14,815	117,215	−26,452	90,763
2005	68,316	−10,533	23,592	−8797	91,909	−19,330	72,579

Results obtained with the CERC formula forced by time series of wave parameter at the breaking point.

It can then be reproached the absence of sand transport data for high-energy wave conditions. This problem corroborates the observations of Schoonees and Theron (1993) and Taborda et al. (1994), who pointed out the challenge that represent the acquisition of field data during high-energy waves. Considering these potential weaknesses, it can be assumed that the values for the annual longshore transport presented in our study are not perfect, but are of the right order of magnitude.

Differences between previous studies and the present one could be rather attributed to some of the weaknesses of previous studies regarding the nearshore wave climate. Previous studies actually took into account average wave parameters while wave-related transport is strongly non-linear. Another weakness in these previous studies concerned the inaccurate determination of wave angle at breaking, which was in the best case determined using a ray model, but most often taken as the offshore wave incidence. In this study, the wave angle at breaking has revealed to be a key parameter that requires being determined very accurately, since the low gradient of the beach and the shallow shoreface cause the waves to break with angles less than 10° and most of the time less than 5°. The last important weakness concerned the use of empirical formulas without any calibration or comparison with field data. In the present study, except for the Kamphuis (1991) formula, empirical parameters have to be adjusted by comparison with field data, as the K_v coefficient for longshore current velocity in the Kaczmarek et al.'s (2005) formula, or the K coefficient in the CERC (1984) formula. This study has also shown that the default values for these parameters, often established from studies on more inclined and barred beaches, were not adapted to the dissipative beach of this study.

Nevertheless, the values computed for the annual longshore transport at St. Trojan beach could appear weak with respect to its energetic wave setting and considering the 193°N shoreline orientation while swells originate from W to NW. Several authors have proposed the main part of the annual longshore transport took place during high-energy events that only represent a few percent of the annual wave climate (Abadie et al., 2006; Sylvester, 1984; Michel, 1997). On the contrary, this study suggests that for St. Trojan beach, energetic swells represent 15–27% of the annual wave climate (category B, Section 5.1) but are responsible for about 40% (Table 4) of the gross annual longshore transport and only 20% of the net annual longshore transport. The relatively weak contribution of energetic swells in the gross annual longshore transport could result firstly from the 30% to 60% amplitude attenuation these swells experience when they propagate over the extended continental shelf and the shallow shoreface in front of Oléron Island (e.g., as during the third tracer experiment; Section 4.1 and Table 1). The second explanation could be related to the systematically close to W direction of these energetic swells (Fig. 2), which cause them to approach the shore with low angles (−4° to 5° of incidence). The even lower contribution of energetic swells in the net annual longshore transport can be related to the fact that swells having an offshore direction of less than about 275°N approach the coast with a weak southward component, which cause the littoral drift to be oriented northward, as during the beginning of the third tracer experiment (Section 4.1 and Fig. 5). Hence, these energetic swells result in a comparable amount of northward and southward transport, which strongly weakens their contribution to the net annual transport (Fig. 10) (Table 4).

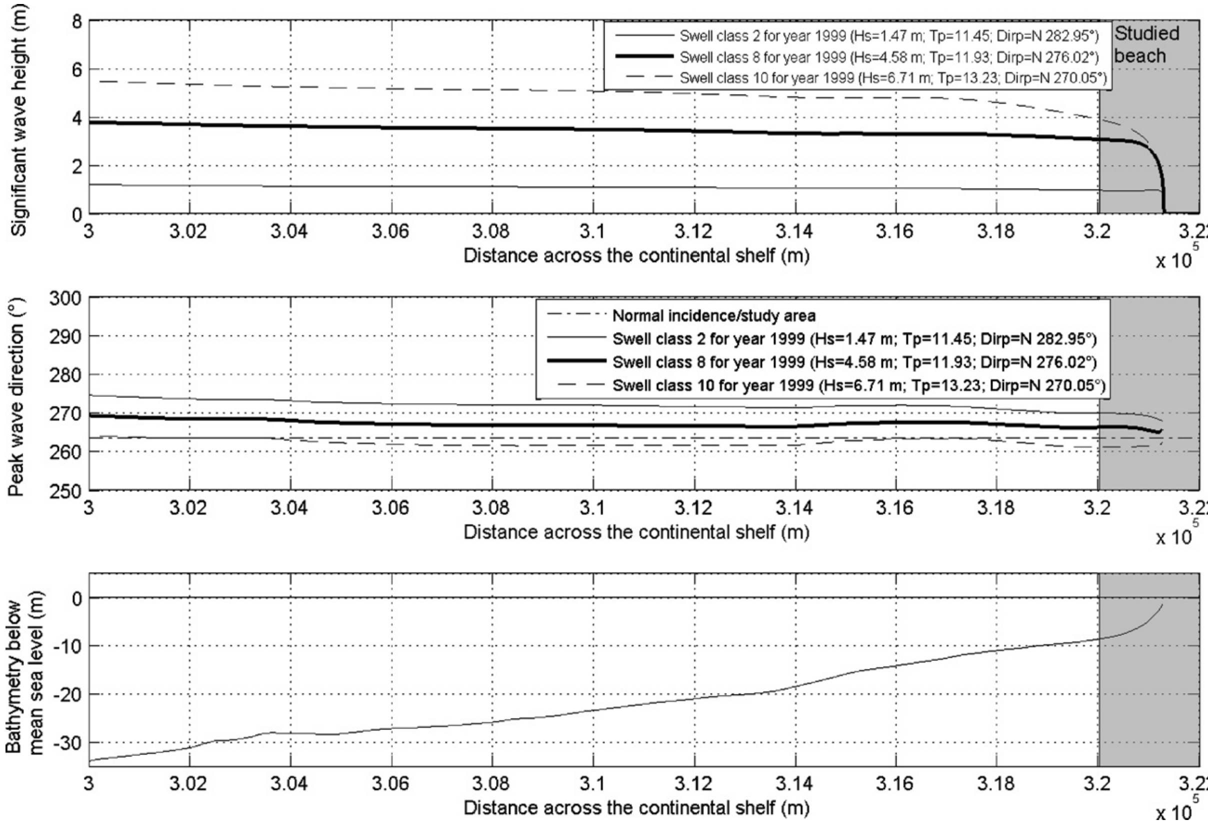

Fig. 10. Swell deformation (refraction and attenuation) during their propagation on the Oléron Island shoreface up to the studied beach, showing that energetic swells are subjected to the strongest deformations.

6. Conclusion

The first objective of this paper was to determine the annual and inter-annual variability of the longshore transport. The first part of the paper presented tracer experiments together with simultaneous hydrodynamic measurements, carried out during three different hydrodynamic settings offering a good representation of the annual wave climate. Hydrodynamic data were used to calibrate numerical simulations of wave propagation, wave-induced currents and sediment transport simulations. Due to the lack of directional wave recorder offshore of the study area, wave data originating from the WW3 model were considered in this study to force a local wave propagation model. The good correlation between the modelled wave parameters (H_s, T_p and Dir_p) obtained from this methodology and field measurements point out the quality of the WW3 data as well as those of the SWAN model. These modelled wave parameters were used to force the hydro-sedimentary model and empirical formulas and have permitted to obtain quite good correlations with measured longshore currents and longshore transports. From these short-term studies, it was assumed that model settings were suitable to compute longshore transport at a larger time-scale.

The nearshore wave climate was then determined by simulating the propagation of offshore waves classes as well as the whole WW3 time series up to the studied beach. A contrasting situation was evidenced between winters characterised by energetic frontal waves and summers characterised by less energetic but more oblique waves. This nearshore wave climate was used to force both the hydro-sedimentary model and empirical formulas and to compute the annual and inter-annual longshore transports. Results obtained from this methodology suggested values for the annual longshore transport ranging from $50{,}000 \pm 20{,}000\,m^3$/yr to $140{,}000 \pm 30{,}000\,m^3$/yr, with a strong inter-annual variability. These values were nevertheless 3–10 times less than those proposed in previous studies, which was firstly attributed to the presence of some weaknesses in these studies regarding the forcing wave climate, the determination of the wave incidence and the non-calibration of transport formulas. The relatively low values presented in this study for the net annual longshore transport were explained by a particularly weak contribution of high-energy swells, related to their strong energy attenuation and their quasi-frontal incidence, which results in a comparable amount of transport southward and northward (Table 4).

Finally, the quite good agreement between the values obtained from the different methods demonstrates the validity of the wave climate classification method. Using this method offers the unique advantage of computing longshore transport over large period of time with reasonable CPU times, which is determinant when using a hydro-sedimentary numerical model.

The overall methodology presented in this study for estimating the annual longshore transport has permitted to obtain unpublished results and should be tested in other places, namely to re-examine some of the values that originate from studies that were conducted with restricted numerical and experimental means.

Acknowledgements

The first author was funded by the European Commission through a Marie Curie Intra-European Fellowship (contract IMMATIE MEIF-CT-2006-041171). Stéphane Recoura, Pascal Tiphaneau, Jonathan Allard and André are greatly thanked for their help during fieldwork. Thank are due to Delft hydraulics for making available their SWAN model and to Dr. David Johnson for his

DIWASP Matlab routines. The estuarine and coastal division of LNEC is thanked for permitting to use the computational resources, which enabled to perform more than 26,000 SWAN runs. The authors also wish to thank the US National Center of Environmental Prediction for making available outputs of the WAVEWATCH III model. Thanks are also due Rodrigo Pedreros and Deborah Idier from BRGM, for providing the 1 month directional wave data acquired to the north of Oléron Island and one part of the WW3 data at the earliest stage of this study. Finally, the comments of the editor David Huntley and those of two anonymous reviewers substantially improved this manuscript and were greatly appreciated.

References

Abadie, S., Butel, R., Dupuis, H., Brière, C., 2005. Paramètres statistiques de la houle au large de la côte Sud-aquitaine. Comptes Rendus Géosciences 337, 769–776.
Abadie, S., Butel, R., Mauriet, S., Morichon, D., Dupuis, H., 2006. Wave climate and longshore drift on the South Aquitaine Coast. Continental Shelf Research 26 (16), 1924–1939.
Bagirov, A.M., Rubinov, A.M., Yearwood, Y., 2002. A global optimization approach to classification. Optimization and Engineering 3, 129–155.
Bailard, J., 1981. An energetic total load transport model for plane sloping beach. Journal of Geophysical Research (C) 86, 10938–10954.
Bailard, J.A., 1984. A simplified model for longshore sediment transport. In: Proceedings of the 19th Coastal Engineering Conference, ASCE, Cap Town, South Africa, pp. 1454–1470.
Balouin, Y., Howa, H., Pedreros, R., Michel, D., 2005. Longshore sediment movements from tracers and models, Praia do Faro, South Portugal. Journal of Coastal Research 22, 146–156.
Battjes, J.A., 1975. Modeling turbulence in the surf zone. In: Symposium on Modeling Techniques: Second Annual Symposium of the Waterways, Harbors, and Coastal Engineering Division of ASCE, vol. 2. ASCE, New York, pp. 1050–1061.
Battjes, J.A., Stive, M.J.F., 1985. Calibration and verification of a dissipation model for random breaking waves. Journal of Geophysical Research 90 (C5), 9159–9167.
Battjes, J.A., Janssen, J.P.F.M., 1978. Energy loss and set-up due to breaking of random waves. In: Proceedings of the 16th International Conference on Coastal Engineering, ASCE, pp. 569–587.
Baxères, P., 1978. Etude morphologique et sédimentologique de la côte Atlantique de la pointe Sud d'Oléron à la pointe de la Coubre (France). Unpublished Ph.D. Thesis, University of Bordeaux I, 190pp.
Bellessort, B., Migniot, C., 1987. De l'estuaire de la Loire à l'estuaire de la Gironde, le catalogue sédimentologique des côtes de françaises, côtes de la Manche et de l'Atlantique, de la Baie du Mont-Saint-Michel à la frontière Espagnole. Collection de la Direction des Etudes et recherches d'électricité de France, Ed. Eyrolles, 559pp.
Bertin, X., Chaumillon, E., Weber, N., Tesson, M., 2004. Morphological evolution and time-varying bedrock control of main channel at a mixed energy tidal inlet: the Maumusson inlet, France. Marine Geology 204, 187–202.
Bertin, X., Chaumillon, E., Sottolichio, A., Pedreros, R., 2005. Tidal inlet response to sediment infilling of the associated bay and possible implications of human activities: the Marennes-Oléron Bay and Maumusson Inlet, France. Continental Shelf Research 25, 1115–1131.
Bertin, X., Castelle, B., Anfuso, G., Ferreira, O., 2008. Improvement of sand activation depth prediction under oblique wave breaking. Geo-Marine Letters 28 (2), 65–75.
Bonneton, P., 2001. A note on wave propagation in the inner surf zone. Comptes rendus de l'académie des Sciences 329 (SIIb), 27–33.
Booij, N., Ris, R.C., Holthuijsen, L.H., 1999. A third generation wave model for coastal regions. Part I: Model description and validation. Journal of Geophysical Research 104, 7649–7666.
Butel, R., Dupuis, H., Bonneton, P., 2002. Spatial variability of wave conditions on the French Atlantic coast using in situ data. Journal of Coastal Research 36 (SI), 96–108.
Castelle, B., Bonneton, P., Butel, R., Dupuis, H., 2005. Morphodynamic modeling of nearshore crescentic bar dissymmetry on an open coast: Aquitanian Coast, France. In: Proceedings of the Coastal Dynamics '05 (CD-ROM), Barcelona, ASCE, 11pp.
Castelle, B., Bonneton, P., Sénéchal, N., Dupuis, H., Butel, R., Michel, D., 2006a. Dynamics of wave-induced currents over an alongshore non-uniform multiple-barred sandy beach on the Aquitanian Coast, France. Continental Shelf Research 26, 113–131.
Castelle, B., Bonneton, P., Butel, R., 2006b. Modeling of crescentic pattern development of nearshore bars, Aquitanian Coast, France. Comptes Rendus Geosciences 338, 795–801.
CERC, 1984. Shore Protection Manual, fourth ed. US Army Engineer Waterways Experiment Station, Coastal Engineering Research Center, US Government Printing Office, Washington, DC.
Ciavola, P., Taborda, R., Ferreira, Ó., Dias, J.M.A., 1997. Field measurements of *Longshore* sand transport and control processes on a Steep Meso-Tidal Beach in Portugal. Journal of Coastal Research 13, 1119–1129.
Dowing, J.P., Sternberg, R.W., Lister, C.R.B., 1981. New instrumentation for the investigation of sediment suspension processes in the shallow marine environment. Marine Geology 42, 19–34.
Ferreira, Ó., Ciavola, P., Taborda, R., Bairros, M., Dias, J.A., 2000. Sediment mixing depth determination for steep and gentle foreshores. Journal of Coastal Research 16, 830–839.
Hoefel, F., Elgar, S., 2003. Wave-induced sediment transport and sandbar migration. Science 299 (5614), 1885–1887.
Idier, D., Predreros, R., Oliveiros, C., Sottolichio, A., Choppin, L., Bertin, X., 2006. Importance de la houle dans la dynamique hydro-sédimentaire des Pertuis Charentais. Comptes Rendus Geosciences 338, 718–726.
Ingle, J.C., 1966. The Movement of Beach Sand. Elsevier, New York, 221pp.
Inman, D.L., Chamberlain, T.K., 1959. Tracing beach sand movement with irradiated quartz. Journal of Geophysical Research 64, 41–47.
Johnson, D., 2002. DIWASP, a directional wave spectra toolbox for MATLAB®: user manual. Research Report WP-1601-DJ (V1.1), Centre for Water Research, University of Western Australia, 18pp.
Kaczmarek, L.M., Ostrowski, R., Pruszak, Z., Rozynski, G., 2005. Selected problems of sediment transport and morphodynamics of a multi-bar nearshore zone. Estuarine, Coastal and Shelf Science 62, 415–425.
Kamphuis, J.W., 1991. Alongshore sediment transport rate. Journal of Waterway, Port, Coastal and Ocean Engineering 117 (6), 624–640.
Kirkpatrick, S., Gelatt, C.D., Vecchi, M.P., 1983. Optimization by simulated annealing. Science 220, 671–680.
Komar, P.D., Inman, D.L., 1970. Longshore sand transport on beaches. Journal of Geophysical Research 75, 5914–5927.
Kraus, N.C., Isobe, M., Igarashi, H., Sasaki, T.O., Horikawa, K., 1982. Field experiments on longshore sand transport in the surfzone. In: Proceedings of 18th Coastal Engineering Conference, Cape Town, South Africa, ASCE, pp. 970–988.
Kraus, N.C., 1985. Field experiment on vertical mixing of sand in the surf zone. Journal of Sedimentary Petrology 55, 3–14.
Levoy, F., Anthony, E., Barusseau, J.P., Howa, H., Tessier, B., 1998. Morphodynamique d'une plage macrotidale à barres. Comptes Rendus de l'Académie des Sciences 327, 811–818 Paris.
Lin, P., Liu, P.L.F., 1998. A numerical study of breaking waves in the surf zone. Journal of Fluid Mechanics 359, 239–264.
Liu, P., Dalrymple, R., 1978. Bottom frictional stresses and longshore currents due to waves with large angle of incidence. Journal of Marine Research 36, 357–375.
Long, B.F., Drapeau, G., 1985. Transport sédimentaire littoral: compte rendu des expériences de traçage durant le programme E.S.C.L. Canadian Coastal Sediment Study, pp. 287–300.
Madsen, O., Poon, Y.-K., Graber, H., 1988. Spectral wave attenuation by bottom friction: theory. In: Proceedings of the 21st International Conference on Coastal Engineering, pp. 492–504.
Masselink, G., Anthony, E.J., 2001. Location and height of intertidal bars on macrotidal ridge and runnel beaches. Earth Surface Processes and Landforms 26, 759–774.
Masselink, G., Hegge, B., 1995. Morphodynamics of meso- and macrotidal beaches: examples from central Queensland, Australia. Marine Geology 129, 1–23.
Masselink, G., Short, A.D., 1993. The effect of tide range on beach morphodynamics and morphology: a conceptual beach model. Journal of Coastal Research 9, 785–800.
Michel, D., 1997. Evolution Morphodynamique d'un Littoral Sableux Situé à l'Aval d'une Embouchure Lagunaire. Unpublished Ph.D. Thesis, University of Bordeaux 1, 162pp.
Osborne, P.D., Vincent, C.E., 1996. Vertical and horizontal structure in suspended sand concentration and wave induced fluxes over bedforms. Marine Geology 131, 195–208.
Park, J.-Y., Wells, J.T., 2005. Longshore transport at Cap Lookout, North Carolina: shoal evolution and the regional sediment budget. Journal of Coastal Research 21, 1–17.
Pedreros, R., Howa, H.L., Michel, D., 1996. Application of grain size trend analysis for the determination of sediment transport pathways in intertidal areas. Marine Geology 135, 35–49.
Philipps, O., 1977. The Dynamics of the Upper Ocean. Cambridge University Press.
Pruszak, Z., Zeidler, R.B., 1994. Sediment transport in various time scales. In: Proceedings of the 24th ICCE, ASCE, New York, pp. 2513–2526.
Russel, P.E., 1993. Mechanisms for beach erosion during storms. Continental Shelf Research 13, 1243–1265.
Schoonees, J.S., Theron, A.K., 1993. Review of the field-data base for longshore sediment transport. Coastal Engineering 19, 1–25.
Smith, E.R., Wang, P., Zhang, J., 2003. Evaluation of the CERC Formula using large-scale model data. In: Proceedings of the Coastal Sediment 2003, Clearwater.
Svendsen, I., Petrevru, U., 1996. Surf-Zone Hydrodynamics, Advances in Coastal and Ocean Engineering, vol. 2. World Scientific, Singapore.
Sylvester, R., 1984. Fluctuation in littoral drift. In: Proceedings of the 19th Coastal Engineering Conference, pp. 1291–1305.
Taborda, R., Ferreira, O., Dias, J.M.A., Moita, P., 1994. Field observations of the longshore transport in an high energy environment. In: Proceedings of the Littoral 94 Conference, Lisbon, Portugal, pp. 479–487.
Tolman, H.L., 2002. User manual and system documentation of WAVEWATCH-III version 2.22. NOAA/NWS/NCEP/OMB. Technical Note 222, 133pp.

Tolman, H.L., Balasubramaniyan, B., Burroughs, L.D., Chalikov, D.V., Chao, Y.Y., Chen, H.S., Gerald, V.M., 2002. Development and implementation of wind generated ocean surface wave models at NCEP. Weather and Forecasting 17, 311–333.
Tonk, A., Masselink, G., 2005. Evaluation of longshore transport equations with OBS sensors, streamer traps and fluorescent tracer. Journal of Coastal Research 21, 915–931.
US Army Corps of Engineers, 1998. Longshore Sediment Transport. Coastal Engineering Manual, Part III, Chapter 2, 109pp.
Vila-Concejo, A., Ferreira, O., Ciavola, P., Matias, A., Dias, J.M.A., 2004. Tracer studies on the updrift margin of a complex inlet system. Marine Geology 208, 43–72.
White, T.E., 1998. Status of measurement techniques for coastal sediment transport. Coastal Engineering 35, 17–45.
White, T.E., Inman, D.L., 1989. Transport determination by tracers. In: Seymour, R.J. (Ed.), Nearshore Sediment Transport. Plenum Press, New York, pp. 115–128.
Wright, L.D., Chappel, J., Thom, B.G., Bradshaw, M.P., Cowell, P., 1979. Morphodynamics of reflective and dissipative beach and inshore systems: South-Eastern Australia. Marine Geology 32, 105–140.